



# Large field Digital Image Plane Holography with a double cavity high speed laser

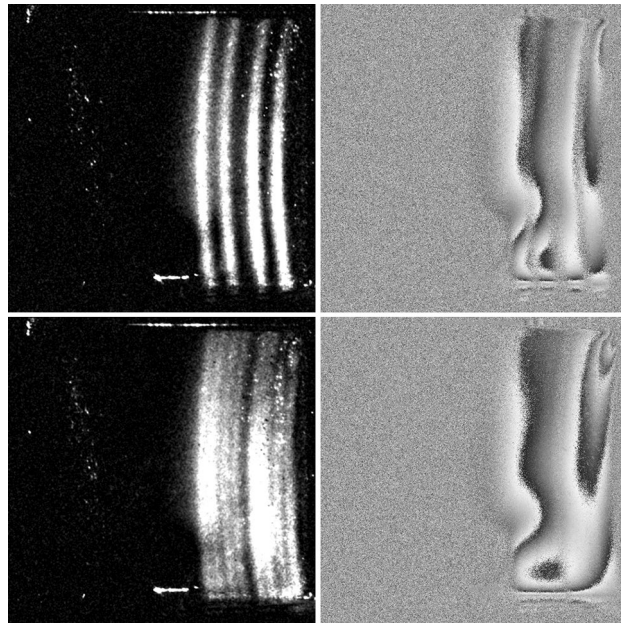
Julia Lobera<sup>1</sup> · M<sup>a</sup> Pilar Arroyo<sup>1</sup> · Eva M<sup>a</sup> Roche<sup>1</sup> · Nieves Andrés<sup>1</sup> · Irene Sancho<sup>2</sup> · Antón Vernet<sup>2</sup> · Jordi Pallarés<sup>2</sup> · Virginia Palero<sup>1</sup> 

Received: 9 May 2022 / Revised: 18 July 2022 / Accepted: 18 August 2022 / Published online: 11 September 2022  
© The Author(s) 2022

## Abstract

The three velocity components in a fluid plane can be measured by applying Digital Image Plane Holography. This technique is limited by the laser coherence length, which reduces its application with high speed lasers that, generally, have a very short coherence length. In addition, the use of a double cavity can also imply a small wavelength difference between the two laser beams. In this work, we present an improved Optical Path Length Enlarging Device that allows the velocity measurement, in a 2D field whose width is four times larger than the laser coherence length. The optical set-up and the procedure for measuring in a larger field (ten times the laser coherence length) were optimized, and the issues derived from the laser spatial and temporal coherence and wavelength changes were analyzed and solved. Digital Image Plane Holography with the Optical Path Length Enlarging Device and Particle Image Velocimetry were applied for measuring the whole velocity field in the central plane of a cylindrical cavity with a rotating lid, for two Reynolds numbers (800 and 2000), showing both of them a very good agreement with the numerical simulations.

## Graphical abstract



✉ Virginia Palero  
palero@unizar.es

Extended author information available on the last page of the article

## 1 Introduction

Digital holography (Schnars and Jüptner 2005; Arroyo and Hinsch 2008; Katz and Sheng 2010) is a technique widely applied in many fields, and, in particular, to characterize fluid flows. In digital holography the light scattered by the object interfere in a digital sensor with a reference beam. Therefore, both the amplitude and the phase of the object wave are captured. Two are the most used configurations: the in-line and the off-axis holography.

In digital in-line holography, a translucent object is usually illuminated with a collimated beam. The light scattered by the object forms the so-called object beam and the unscattered light, forms the reference beam. This configuration presents several disadvantages. One is the well-known twin image problem (Denis et al. 2008; Ooms et al. 2008; Palero et al. 2014): the object virtual and real images are not fully separated when the hologram is reconstructed, which add noise to the reconstruction. The second drawback is the low system aperture, as the light scattered by the particles presents a narrow lobe in the forward direction. Thus, the reconstructed particle images length along the observation direction is several times bigger than the real size. As a consequence, the accuracy in determining the position of the particle along the optical axis and the spatial resolution decrease. Another drawback is the flow cross-sectional dimension that can be recorded, which is limited by the size of the camera sensor, typically a few square centimeters. Despite these drawbacks, several authors (Lebon et al. 2016; Chen et al. 2017; Tolui et al. 2017; López et al. 2020) have shown that digital in-line holography is a feasible technique for measuring the three velocity components (3C) in a volume (3D), or to obtain the particle size distribution (Gómez-Climente et al. 2022).

In digital off-axis holography (Sheng et al. 2003; Verrier and Atlan 2011) the laser beam is separated in two: the illuminating and the reference beams. The light scattered by the illuminated object forms the object beam. For this beam to interfere at the sensor with the reference beam, the optical path of both beams must be matched within the limits of the laser coherence length.

Digital Image Plane Holography (DIPH) (Lobera et al. 2003, 2004a), an off-axis holographic technique, has shown its applicability for particle sizing (Palero et al. 2005, 2007) and for the measurement of the whole velocity field in a fluid plane (Palero et al. 2010).

DIPH allows the measurement of the three velocity components (3C) in a fluid plane (2D) that is imaged onto a digital camera. This object intensity distribution interferes in the camera sensor with an off-axis reference beam, making a so-called image hologram. Series of holograms

are recorded with a suitable time interval ( $\Delta T$ ) between them. The velocity is obtained from the analysis of the numerically reconstructed complex amplitude distributions from holograms recorded consecutively. The in-plane components can be obtained from the intensity distribution, while the out-of-plane component is extracted from the phase distribution, using an interferometric analysis.

This holographic technique is suitable for the analysis of liquid confined flows, which are of interest for basic research and for many technological applications. DIPH presents several advantages compared with photographic techniques, such as Stereoscopic Particle Image Velocimetry (Arroyo and Greated 1991). Stereoscopic PIV is an extension of PIV (Raffel et al. 1998) that measures the three velocity components in a fluid plane by combining the projection of the velocity field over two cameras that visualize the fluid plane from two different directions. Stereoscopic PIV requires a large optical access that can eventually prevent its application in a confined flow (Palero et al. 2000). Besides, the application in liquid flows is also difficult as the change in the refractive index introduces strong distortions in the images (Prasad and Adrian 1993; Prasad and Jensen 1995).

In DIPH, the size of the recorded fluid plane is limited by the laser coherence length ( $\ell_c$ ). The larger  $\ell_c$ , the larger will be the region that can be recorded with DIPH. Most High Speed lasers have a short temporal coherence length ( $\ell_c \sim 10$  mm in air). Thus only a width of  $\Delta x = \ell_c/n_f$  in a fluid with refractive index  $n_f$  can be recorded. In Palero et al. 2010, we have shown that the laser coherence length can be artificially increased for measuring the velocity field inside a complex geometry brain aneurysm model, whose size was 15 mm. The application of DIPH in a larger area, ten times bigger the coherence length in our particular case, presents new challenges. The spatial coherence, which did not affect the measurements done in Palero et al. (2010), plays here a relevant role since the height of the flow requires expanding more the laminar beam. In addition, we have to solve the problem that arises when the wavelength changes with the energy output of a high speed double cavity laser.

The application of DIPH to the flow generated in a lid-driven cavity has been analyzed. These kinds of flows have a growing interest, as they have a simple geometry and are physically realizable. In contrast, the flow exhibits a relatively complex behavior, especially as the Reynolds number (or for example, the velocity of the lid) is progressively increased (Shankar and Deshpande 2000) Flow features such as corner and longitudinal vortices, three-dimensionality and a progressive transition to turbulence can be analyzed in this simple flow configuration. The flow field in the laminar regime has been characterized numerically and experimentally (Escudier 1984; Spohn et al. 1998; Sancho et al. 2016; Cabeza et al. 2010). The flow exhibits axisymmetric steady vortex breakdown phenomena and, as the rotational Reynolds is increased,

the coexistence of different modes or non-axisymmetric flow structures with certain characteristic frequencies in the velocity signal (Sørensen et al. 2006).

The whole velocity field has been measured (and numerically simulated) in a fluid plane 80 mm wide using only one high speed camera and a double cavity laser. In fact, the method developed in this work allows the measurement of the three velocity components in a plane of a stationary flow of any spatial dimensions. High Speed PIV has been applied for measuring the in-plane velocity components, to increase the numerical aperture of the system, and therefore improve the spatial resolution of the final measurement (Lobera et al. 2004b). The out of plane component has been measured using DIPH.

The experimental results have been compared with numerical simulations obtaining a very good agreement for the three velocity components.

## 2 Digital Image Plane Holography

The recording and analysis of holograms using Digital Image Plane Holography (DIPH) has been explained in detail in previous works (Lobera et al. 2003, 2004a). In order to provide the reader with complete information, the principles are explained in the following. In DIPH, a fluid plane is illuminated with a laser sheet and its image is formed with a lens in a camera sensor (as in PIV), where it interferes with a reference wave, making a so-called image hologram. The reference beam is a divergent wave whose source is located at the same distance from the sensor as the imaging lens aperture. This holographic set-up produces a lensless Fourier transform hologram of the lens aperture with the advantage of allowing an easy isolation of the real image from the virtual image and DC (zero-order interference) terms. Figure 1a shows a schematic representation of the DIPH configuration. The full hologram is not included in this figure, as the object intensity is too low and only the reference contribution will be visible. We show a magnified area of the hologram: from a region where the object and reference beams are interfering, i.e., an area where both beams are coherent.

If  $\tilde{o} = oe^{i\phi_o}$  is the object beam, i.e., the light scattered by the illuminated fluid plane, and  $\tilde{r} = re^{i\phi_r}$  is the reference beam (being  $\phi_o$  and  $\phi_r$  the object and reference phases, respectively), the hologram intensity can be written as:

$$I = o^2 + r^2 + \tilde{r}^* \tilde{o} + \tilde{r} \tilde{o}^* \tag{1}$$

In the spatial domain, these four terms are mixed, but they can be separated in the frequency domain. The Fourier transform of one hologram can be calculated as:

$$\mathfrak{F}\{I\} = r^2\delta(0, 0) + \mathfrak{F}\{o^2\} + \mathfrak{F}\{\tilde{r}^* \tilde{o}\} + \mathfrak{F}\{\tilde{r} \tilde{o}^*\} \tag{2}$$

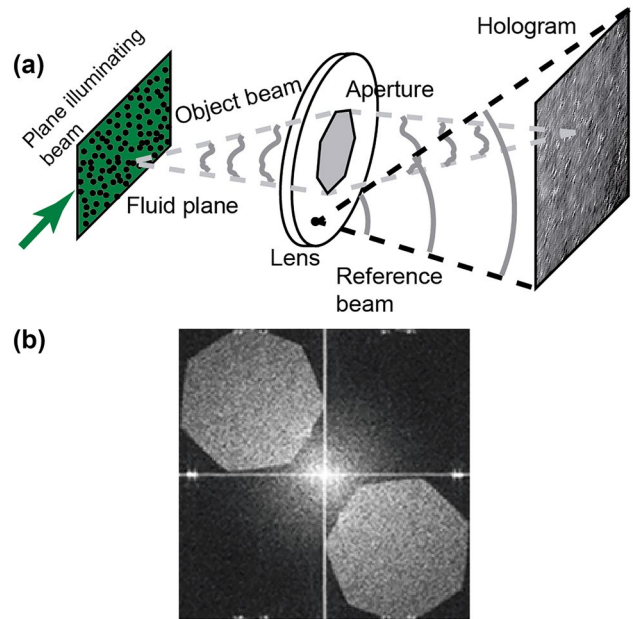


Fig. 1 a Schematic representation of the DIPH configuration; b Fourier Transform intensity of a DIPH hologram

Figure 1 shows the Fourier transform intensity of one of these holograms. The heptagons are the real and virtual images of the lens aperture (the third and fourth terms in Eq. 2), which are completely separated. The DC term contains the Fourier transform of  $o^2$  and  $r^2$ . Now,  $r^2$  is approximately a delta function and generally appears as a bright spot in the Fourier plane center. Also in the center, the object Fourier transform intensity spreads and overlaps slightly with the real and virtual images.

In the reconstruction process, the real image of the lens aperture in the hologram Fourier transform is selected and moved to the center, while the rest is blocked. Then, its inverse Fourier transform, for partially coherent beams, reconstructs a complex amplitude

$$\tilde{a} = |\gamma|roe^{i\phi} \tag{3}$$

where  $|\gamma|$  is the degree of coherence (Lauterborn and Kurz 2003), which will vary along the x and y coordinates of the image with the temporal and spatial coherence of the reference and object beams. From,  $\tilde{a}$  we obtain a reconstructed intensity distribution  $o^2$ , which is like a PIV image. Then it is possible to obtain the in-plane velocity components by correlating pairs of them, separated a time interval  $\Delta T_{PIV}$ . The reconstructed phase distributions,  $\phi = \phi_o - \phi_r$ , can be analyzed by an interferometric approach in order to calculate the out-of-plane velocity component (Rastogi 1994; Andrés et al. 1999; Kreis 2005). If pairs of holograms are recorded with a suitable time interval ( $\Delta T$ ), the subtraction of the two phase distributions ( $\Delta\phi$ ) corresponding to a given hologram

pair, gives a map which is related to the displacement  $\vec{d}$  in  $\vec{K}$  direction such that,

$$\Delta\phi = \vec{K} \cdot \vec{d} = \frac{2\pi}{\lambda} (\vec{u}_o - \vec{u}_i) \cdot \vec{d} \quad (4)$$

where  $\vec{K}$  is known as the sensitivity vector and depends on the observation ( $\vec{u}_o$ ) and illumination ( $\vec{u}_i$ ) directions. Thus, we measure the displacement (and, therefore, the velocity) along the direction of the sensitivity vector. In the DIPH configuration, the phase difference can be expressed as:

$$\Delta\phi = \frac{2\pi}{\lambda} (d_x + d_z)$$

The phase difference maps contain information about the in-plane ( $d_x$ ) and the out-of-plane ( $d_z$ ) displacement, and the corresponding velocity components. Once  $d_x$  is known,  $d_z$  can be obtained directly.

### 3 Experimental set-up

We will analyze the stationary, laminar flow in the central plane of a cylindrical cavity made of polymethyl methacrylate (PMMA, refractive index,  $n_{\text{PMMA}} = 1.495$ ) with an inner diameter  $D = 2R = 80$  mm (Sancho et al. (2016)). The aspect ratio of the cavity is set to  $H/R = 2$ . Its top wall is rotating with an electronically controlled DC motor that operates at different angular velocities. The fluid is a water-glycerin (60% v/v glycerin) solution with kinematic viscosity  $\nu \sim 10^{-5}$  m<sup>2</sup>/s, density  $\rho \sim 1100$  kg/m<sup>3</sup>, and refractive index  $n_f = 1.425$ . This fluid has been seeded with 20  $\mu\text{m}$  Orgasol particles. The flow Reynolds number, based on the maximum linear velocity of the lid and the radius of the cavity, varies from 800 to 2300. In order to avoid the aberration in the image that appears when an object is visualized through a curved surface, the cylinder is enclosed in a rectangular case made also of PMMA, and filled with the water-glycerin solution that works as index-matching liquid.

A high speed double cavity New Wave Pegasus laser ( $\lambda = 527$  nm, energy per pulse = 10 mJ at 1000 Hz) is used as a light source. The laser beam is divided into two beams with a wedge placed very close to the laser output (Fig. 2). Both beams are guided close to the measurement area by two optical arms. The strongest beam is shaped into a laser sheet that illuminates a central plane in the cylindrical cavity (illumination beam). This laser sheet is produced by a set of spherical lenses, which focuses the beam in the fluid region, and a cylindrical lens, which expands the beam in vertical. The weakest beam, which is used for the reference beam, passes through an Optical Path Length Enlarging Device (OPLED) before entering its optical guiding arm. After this, a lens expands it so it will cover the whole camera sensor.

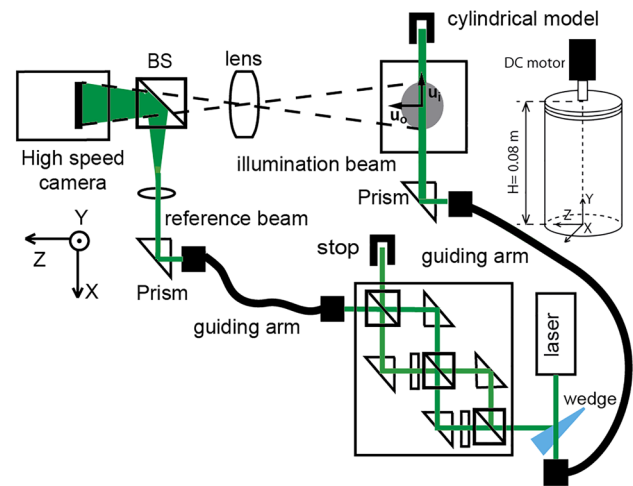


Fig. 2 Experimental set-up

A high speed CMOS camera (Fastcam SA2, 16 bits,  $2048 \times 2048$ , pixel size of  $10 \mu\text{m} \times 10 \mu\text{m}$ , 1000 fps) and a photographic lens ( $f = 60$  mm) are used to record the fluid plane with a magnification of  $M = 0.216$ , at 1000 fps. The entire set-up is placed on an optical table to dampen possible vibrations. Each laser is fired at half this rate (500 pulses/s) giving a time interval  $\Delta T_{\text{PIV}} = 2$  ms, which is suitable for a PIV analysis (in-plane components). The time interval between the pulses from both lasers,  $\Delta T$ , is typically a few  $\mu\text{s}$ , which is the time interval suitable for the interferometric analysis (out-of-plane component).

Holograms were recorded with  $f\# = 32$ , which is the maximum aperture allowed by the Fourier transform hologram arrangement. PIV images were recorded afterward by just blocking the reference beam and increasing the lens aperture up to  $f\# = 8$ .

In the following we will show the reconstructed amplitude and phase distributions obtained in different conditions in order to prove our technique. All of these are 2D images, where the horizontal direction corresponds to the X axis and the vertical direction to the Y axis. We are showing complete images of  $2048 \times 2048$  pixels<sup>2</sup>, which with our magnification means that we are imaging a region of  $94.8 \times 94.8$  mm<sup>2</sup> in the reactor.

#### 3.1 Optimizing the effective temporal coherence length

Let us first describe the requirements for setting up the large field DIPH, when using a small coherence length laser. First of all, the optical path lengths for both the object and the reference beams have to be matched within the temporal coherence length at a chosen point in the camera sensor. It requires knowing the length and refraction index of all the media each beam is passing through from the beam sampling



wedge (Fig. 2) in front of the laser until the combining beam splitter (BS) in front of the camera sensor. The final adjustment is made by displacing the guiding arm outputs and/or the final prisms (reference and object prims in Fig. 2) in both beams. Beam polarization is also an important issue in any holographic technique. By properly placing the articulated parts of the arm, the output beams are vertically polarized. This also ensures that both beams have either the same orientation or that they are inverted or rotated 180°. This orientation will be considered again in Sect. 3.3 when we will discuss the spatial coherence issues.

Enlarging the effective temporal coherence length also helps in matching the object and reference beams optical path lengths. For this work, we have developed an improved version (Fig. 3) of the OPLED proposed previously in Palero et al. (2010). As before, the reference beam entering BS1 is splitted, redirected and recombined by an ensemble of beamsplitters and prisms so two sets of four beams, which follow different paths in the OPLED, output the beamsplitter BS3. In the present system, where not only the beamsplitters (BS1–BS3) but also the prisms (P1–P4) are identical, the four beams (R1–R4) will have the same optical path length if the glass plates (W1 and W2) are removed. Thus, the four beams will interfere producing a pattern as in a Mach-Zehnder interferometer.

This is very important as it allows a perfect overlapping of the four reference beams that was not possible with the previous OPLED. As the four beams have the same optical path length, their parallelism and overlapping can be optimized by precisely controlling the tilt and position of the prisms until all the fringes are removed from that interference pattern. If no extra optical length is added the four reference beams will interfere with the same object area.

In order to enlarge the interference area, extra optical path lengths can be added to any of the four reference beams by using plane parallel optical windows (glass plates) with different widths. The extra optical path length introduced by each window will be,  $L_i = (n_g - n_a) \cdot w_i$ , being  $n_a$  and  $n_g$  the air and glass refractive indexes respectively, and  $w_i$  the optical window width. With only two glass plates, placed as shown in Fig. 3a, the four reference beams (R1, R2, R3 and R4) will have increasingly longer optical path lengths. W1 introduces a difference of  $L_1$  between R2 and R1 (and between R4 and R3) while W2 introduces  $L_2$  between R3 and R1 (and between R4 and R2). When  $L_1 = \ell_c$  and  $L_2 = 2 \ell_c$ , the final reference beam will allow recording a maximum object length of  $4 \ell_c n_f$ , being  $\ell_c$  the laser temporal coherence length in air and  $n_f$  the fluid refractive index.

The physical paths for each reference beam, which are color-coded in Fig. 3a, show the system versatility as one, two (R1 + R2 or R3 + R4 or R1 + R3 or R2 + R4) or the four beams can be chosen as the output reference beam by blocking the corresponding paths. Figure 3b shows that only R1

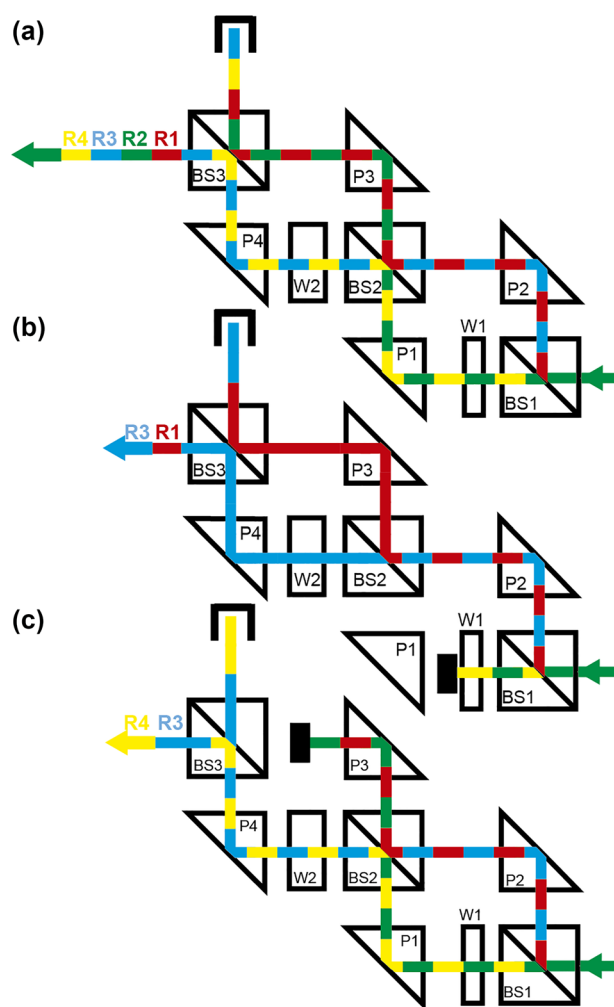


**Fig. 3** Schematics of the Optical Path Length Enlarging Device (OPLED). BS1–BS3: non-polarizing 50/50 beam splitters, P1 to P4: right angle prisms, W1 and W2: glass plates. **a** Colors are used to show the beam splitting/recombination. Different reference beam output the OPLED **b** an obstacle between W1 and P1 blocks R2 and R4, allowing R1 and R3 to pass; **c** an obstacle between P3 and BS3 blocks R1 and R2, allowing R3 and R4 output the system

and R3 will output the OPLED if an obstacle is located between W1 and P1, while in Fig. 3c, an obstacle between P3 and BS3 blocks R1 and R2, so R3 and R4 output the OPLED. From now on, we will consider these four reference beams to be a unit called RS.

### 3.2 Hologram processing

Let us now explain the procedure we have developed for improving the information obtained from the recorded holograms. First of all, we systematically record series of  $N$  hologram pairs ( $A$  and  $B$ ) and one pair of the corresponding reference beams (by just blocking the object beam). Let us refer to the hologram intensities as  $I_{nA}, I_{nB} (n = 1, 2, 3, \dots, N)$

to the reference beam intensities as  $I_{rA}$  and  $I_{rB}$ , where  $A$  and  $B$  refer to the two different lasers. The Fourier transform of one hologram is calculated in order to obtain the size and position of the aperture images. Since the intensity of the object beam is much smaller than the intensity of the reference beam, i.e.,  $o \ll r$ , the  $r^2 \delta(0, 0)$  term of Eq. 2 is removed by calculating  $\mathfrak{F}\{I_{nA} - I_{rA}\}$ .

Now, with the procedure described in Sect. 2 applied to the holograms  $I_{nA}$  and  $I_{nB}$ , the complex amplitudes  $\tilde{a}_{nA} = |\gamma_A| r_A o_{nA} e^{i\phi_{nA}}$  and  $\tilde{a}_{nB} = |\gamma_B| r_B o_{nB} e^{i\phi_{nB}}$  are reconstructed.  $r_A$  and  $r_B$  are also calculated with the same procedure when applied to the reference beams  $I_{rA}$  and  $I_{rB}$  with the same size selecting aperture but placed in the Fourier plane center. Finally, a resultant complex value (Palero et al. 2010) with an average amplitude  $a_o$  and phase difference  $\Delta\phi$  is calculated as

$$\tilde{a}_o(x, y) = \frac{1}{N} \left[ \sum_{n=1}^N \frac{|\gamma_A| o_{nA}(x, y) + |\gamma_B| o_{nB}(x, y)}{2} \exp[j(\phi_{nB}(x, y) - \phi_{nA}(x, y))] \right] = a_o e^{i\Delta\phi} \quad (5)$$

The amplitude and the phase difference for only one pair of holograms ( $N=1$ ) are shown in Fig. 4a, b. The amplitude and phase difference maps show the width, height and position of the coherence regions. Although the results with one pair of holograms are quite good, they are a bit too noisy. A higher seeding could provide more continuous information and, thus, less noisy results. However, a higher seeding will

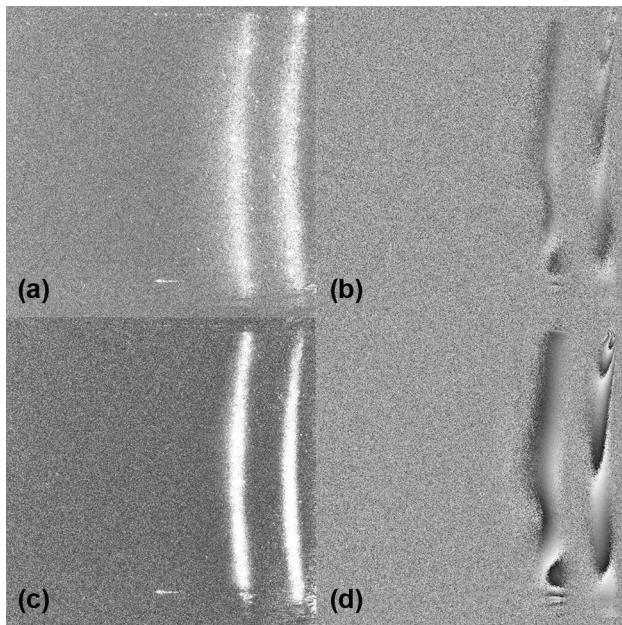


**Fig. 4** Results from 1 pair (a, b) and 20 pairs (c, d) of holograms recorded with R1 and R3. a, c Reconstructed amplitude distribution, b, d reconstructed phase difference map

also increase the scattering of the illuminating beam, which will not be able to travel through the whole fluid volume without significantly increasing its width. This is especially important in large field experiments. For stationary flows, as in our case, an alternative way to increase the apparent seeding is to use a series of  $N$  pairs of holograms. Figure 4c, d shows the amplitude and phase difference with  $N=20$  pairs of holograms. We have checked that 10–20 hologram pairs produce a good enough noise reduction.

In the next step, the complex  $\tilde{a}_o(x, y)$  is spatially filtered. The resultant intensity ( $I_o = a_o^2$ ) and phase difference ( $\Delta\phi$ ) maps are shown in Fig. 5a, b respectively, for  $N=1$  (top) and  $N=20$  (bottom) pairs of holograms. It can be seen two curved coherence stripes, corresponding to two OPLED outputs (R1 and R3). The curved central line of each of these two regions is the null optical path length difference (OPD) line, i.e., the optical path length for the object beam at these points matches the optical path length for the corresponding reference beams. The null OPD line curvature is partially due to the vertically divergent illuminating beam, which is mostly used for large size flows, since collimating the beam will require a too large diameter lens or some other bulky optics. However, the main contribution comes from the different optical path length for each light ray going from a fluid plane point to its corresponding point in the camera sensor (image plane), due to the large size flow. It produces a displacement on the null OPD line of about 2 mm to the right on the top and the bottom of the fluid as compared with the half height point. Let us note that the amplitude (Fig. 4a, c) and intensity images (Fig. 5a) are rescaled such that the 5% brightest points are set to the maximum gray level (255) in order to enhance the relevant spatial information. This type of images is presented in this way all through the paper.

For quantitative information, the values along a horizontal line at the cavity half height ( $Y=40$  mm), for an  $X$  range including only the coherent zone, are plotted (Fig. 5c). The intensity plot (red line) shows the two regions where the degree of coherence is not zero, which are directly related to the laser temporal coherence function. Let us note that the intensity values are in gray levels, although we have chosen to name them arbitrary units (a.u.) since we are not obtaining the real object intensity. The shape of the two separated areas should be similar even if their intensity is different. This is not so when we only use a pair of holograms (Fig. 5c, top) due to a non-uniform object beam, in which strong peaks correspond to bright individual particles. The noise improvement in the intensity and phase difference values obtained from the averaged complex amplitude (Eq. 4) is apparent in the line plot (Fig. 5c, bottom). Now, the shapes of the two intensity profile peaks are quite similar since the influence of the individual bright particles is reduced. In the rest of the paper,  $N=10$ – $20$  is always used.

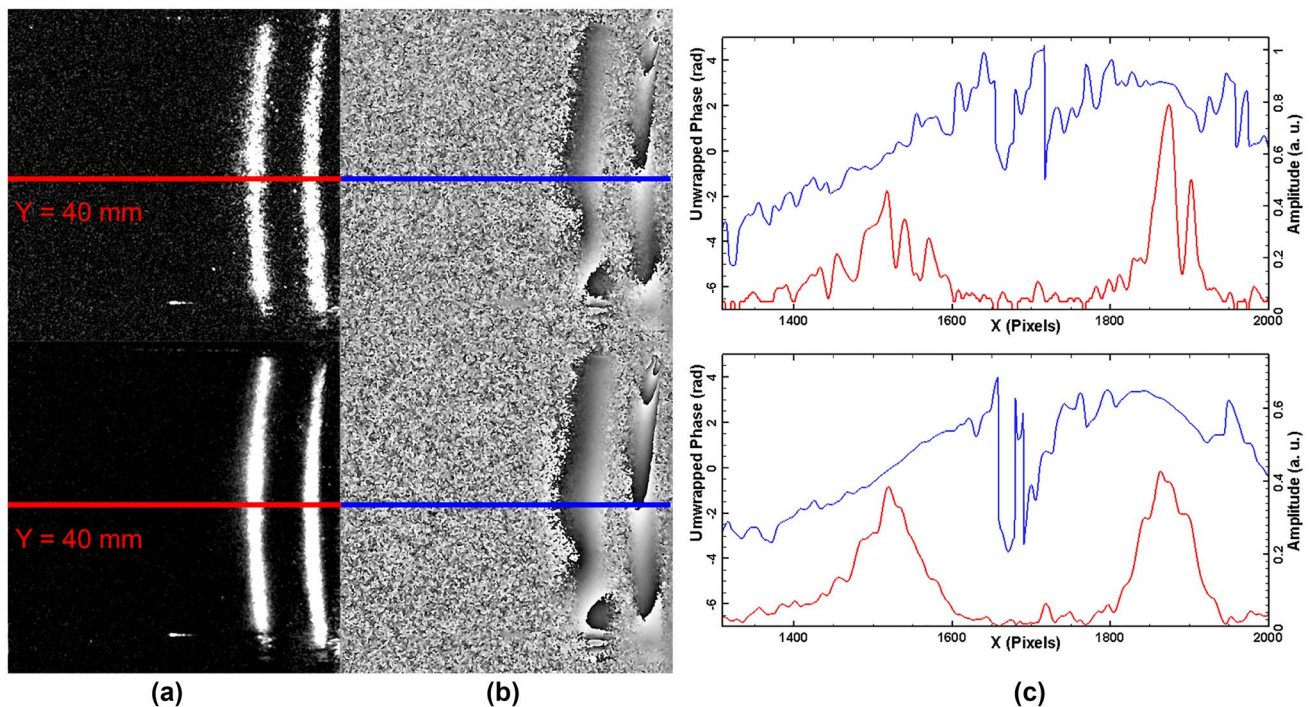


**Fig. 5** Results from the processing of  $N=1$  (top) and  $N=20$  (bottom) hologram pairs recorded with  $R1$  and  $R3$ . **a** Filtered intensity distribution, **b** filtered phase difference map, **c** central line profiles of filtered intensity and phase difference

### 3.3 Optimizing the measurement areas

Optimizing the large field DIPH set-up required to take into account the laser spatial coherence properties, which played no role at all when studying small area flows as in Palero et al. (2010). The laser beam can be considered to originate from an extended light source. The expansion rate and orientation of both, the reference and the illumination beams, have to be well controlled in order to spatially match corresponding points on the camera sensor. Since the laser was linearly polarized, we used the polarization direction to orientate both beams. The articulated parts of the two guiding arms were arranged so that both beams were vertically polarized, which is also the best polarization for maximizing the scattering light from the fluid plane in our set-up. Furthermore, vertical polarization also optimizes the interference between the reference and object beam in our off-axis DIPH set-up.

Figure 6 shows a schematics of the reference and the illumination beams (as seen on the camera sensor) and the resulting intensity maps for several reference beam orientations and/or positions. The points A–D are separated points of the laser beam and are seen as such in the reference beam (Fig. 6b–d). However, they are seen as lines in the illumination beam (Fig. 6a), where they are drawn taking into account the beam divergence. Furthermore, the points A, D

and E overlap in the illumination beam (light sheet) and thus only the line for A is drawn.

As Fig. 6a sketches, the illumination beam, as seen in the camera sensor (black square), is a beam travelling from right to left, diverging in vertical (and converging in depth). One to four are four wavefronts with increasing optical path lengths, which will match the optical path length of the corresponding reference beams. Figure 6b–d sketch the four reference beams, for two different orientations and a vertically displaced position. Figure 6e–g sketch the coherence areas where the object beam (light scatter by the illumination beam) will interfere with the reference beam to form a hologram. Figure 6h–i shows two experimentally reconstructed intensity maps.

There are three requirements for the interference (hologram) to be optimally produced: the two beams have the same polarization (vertical in our case); the OPD between object and reference beam is smaller than the temporal coherence length; and the distance between overlapping points from the two beams is smaller than the spatial coherence length. The temporal coherence requirement implies that there are four regions with interference patterns (1–4), whose width is determined by the temporal coherence length. The spatial coherence requirement implies that there is interference only when there is a spatial matching of both beams, within the spatial coherence length. The polarization requirement implies that only two reference beam



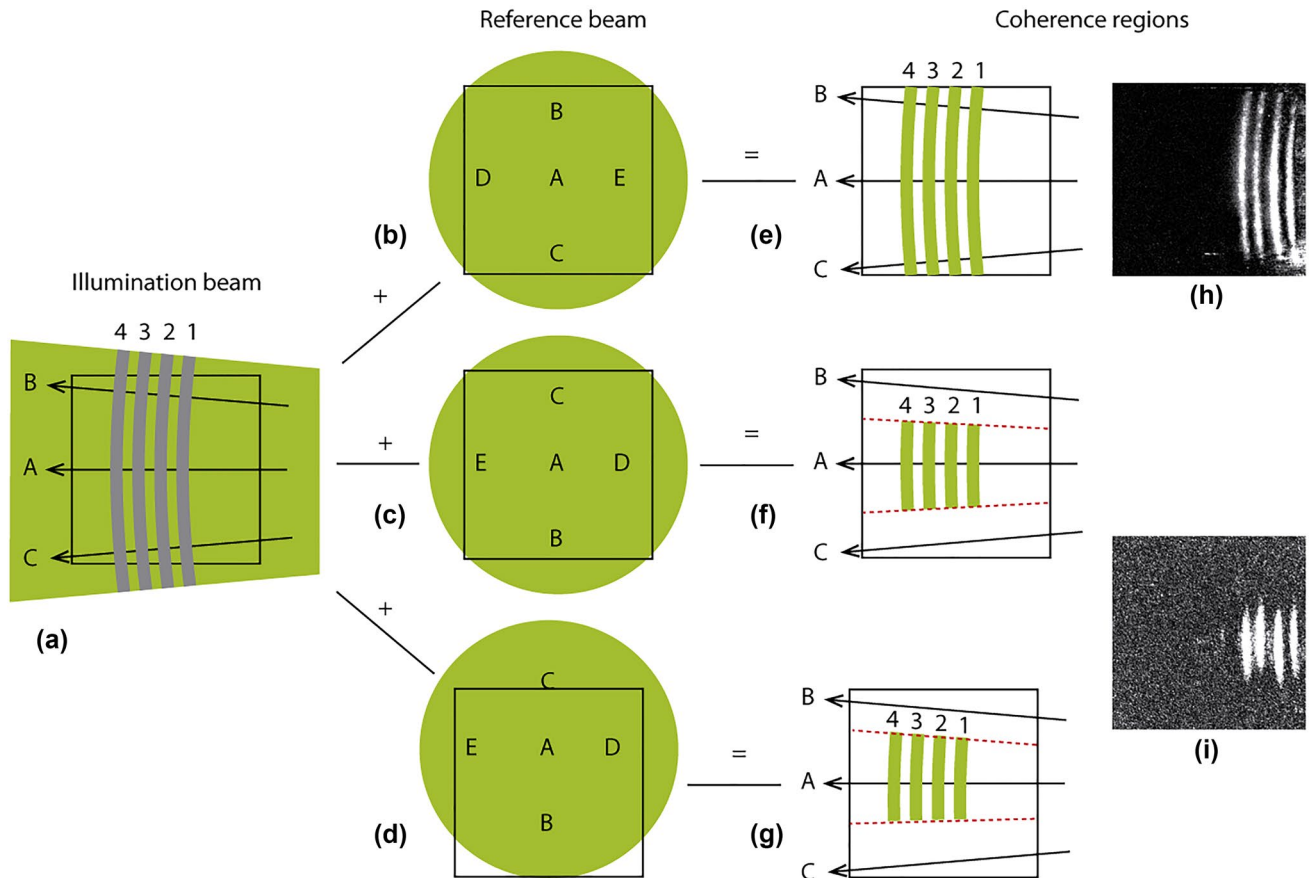


**Fig. 6** Influence of the laser spatial coherence length on the reconstructed information. The illumination (a) and reference (b, c, d) beams are schematically drawn in green in the camera sensor plane; A–D are several points in the laser beam; the red dotted lines show the vertical limits of the coherence regions; the black rectangle shows the sensor size. The reconstructed intensity (e, f, g) is schematically

drawn for the cases of: e non-inverted and well centered reference beam (optimized set-up); f vertically inverted reference beam; g vertically inverted and displaced reference beam; h experimental intensity map for the (e) configuration; i experimental intensity map for the (f) and (g) configurations

orientations are suitable: non-inverted (Fig. 6b), where B is up like in the illumination beam; and inverted (or rotated  $180^\circ$ ), where B is down (Fig. 6c, d).

The optimized set-up (Fig. 6b, e) corresponds to a non-inverted reference beam, where the reference and the illumination beams are perfectly centered in vertical and have about the same height (bigger than the camera sensor). Thus, the source points A, B and C in the illumination beam overlap the same points in the reference beam within the laser spatial coherence length. The height of the reconstructed region is maximized (Fig. 6e, h). In this case, only the temporal coherence limitations remain.

The spatial coherence limitations are more apparent when a vertically inverted reference beam is used (Fig. 6c, d). If the reference beam is vertically centered with respect to the illumination beam (Fig. 6c), the reconstructed region will be centered in A (Fig. 6f, i) and its height, marked with the red-dotted lines, is determined by the laser spatial coherence length. Figure 6i is very illustrative because it also

shows that the reference beams R1 and R3 are vertically misaligned with respect to the reference beams R2 and R4. This situation is sketched in Fig. 6d, g. When the reference beam is displaced upwards by a distance  $d$ , the coherence areas are also displaced upwards by  $d/2$ . It is at this distance, that the two overlapping points come from the same laser beam point; i.e., they are perfectly matched. In this particular case, the displacement was produced by a very small tilt of the prism P1 (or P2) of the OPLED, which is compatible with the long reference beam guiding arm. The same coherence region vertical displacement occurs if the illumination (instead of the reference) beam is vertically displaced.

Thus, with an inverted reference beam, there will always be a region of coherence with good contrast if the OPD is correct, and this can be used for a preliminary alignment. Then, the reference or the illumination beams can be displaced for vertically centering the coherence area. However, with a non-inverted reference beam, any position or size mismatching in vertical will reduce the interference contrast;



i.e., it will degrade the SNR of the reconstructed image. Furthermore, in the extreme case that the spatial mismatching of all the points is bigger than the spatial coherence length, no interference will be observed and no hologram will be obtained, which can be misinterpreted as a wrong adjustment of the OPD.

In our set-up, we can easily switch from an inverted to a non-inverted reference beam by rearranging the end of the reference beam guiding arm. The arrangement with the inverted reference beam is first used for matching the optical path lengths of the reference and object beams because the hologram quality will not depend on the matching of either the beam size or the vertical position. It is also used for optimizing the vertical alignment of the OPLED. The final adjustment of the system is then done with the non-inverted reference beam by optimizing the SNR of the reconstructed image.

Let us now look at the experimental results (Fig. 7) obtained with the optimized set-up (sketched in Fig. 6a, b, e), when using two optical windows in the OPLED with a width of  $w_1 = 15$  mm and  $w_2 = 40$  mm. The reconstructed filtered intensity (Fig. 7a) shows four well separated stripes, corresponding to the four references beams of the RS. These four regions are cut at both ends by the flow cavity horizontal walls, which means the object and the reference beams were interfering in a region whose height was larger than the cavity height (80 mm). We have checked that the four null OPD lines are circular curves with a common center.

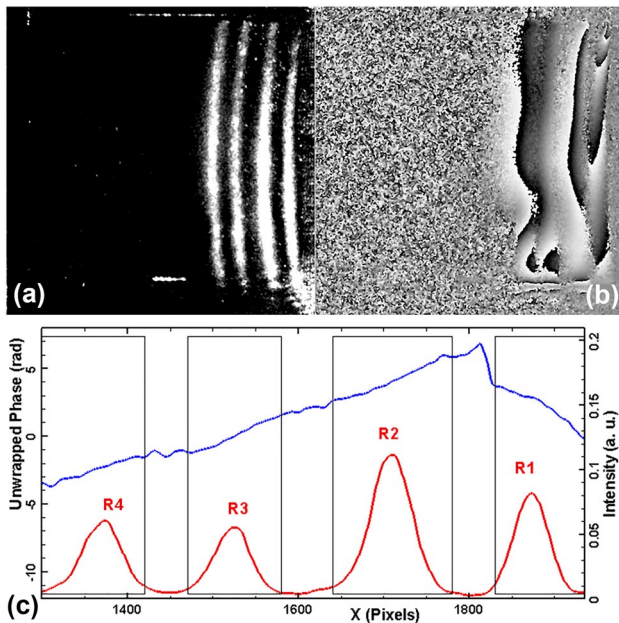


**Fig. 7** Results from a hologram recorded with the RS unit in the final DIPH set-up. **a** Intensity distribution, **b** phase difference map, **c** averaged line profile of filtered intensity (red line) and central line profile of filtered phase difference (blue line)

This center is found to be at  $x = 7385$  pixels,  $y = 1020$  pixels, being the origin  $(x,y) = (0,0)$  at the image upper left corner. In this way, the regions centers,  $x_c$ , at the line  $y = 1020$  pixels have been obtained (Table 1). Since the optical path length for the object beam at these points matches the optical path length for the corresponding reference beams, the OPD between any two reference beams  $R_i$  and  $R_j$  can be calculated as  $OPD_{ij} = n_f(x_{c,j} - x_{c,i})$ . Table 2 shows the results and the nominal values obtained from the  $w_1$  and  $w_2$  values. The differences between measured and nominal values are  $2.7 \pm 0.5$  mm for the beams that go through the first rectangle of the OPLED, and  $2.3 \pm 0.5$  for the beams that go through the second rectangle. This is due to a small misalignment of the OPLED that makes the beams to draw slightly deformed rectangles. It can be seen as a drawback or alternatively as a way to finely tune the  $OPD_{ij}$ 's between the four reference beams. On the present experiments, the resultant  $OPD_{ij}$ 's had roughly the desired values so we choose not to readjust the OPLED.

An estimation of the size of the measurement areas can be obtained from the phase maps (Fig. 7b). Although it will be necessary to unwrap, the phase to measure the out-of-plane component of the velocity, we present the wrapped phase map as the four coherence regions are better appreciated. They are separated by small non coherent areas (phase difference is just noise as in the left of the maps), and some phase jumps between consecutive regions. Some circular curves can also be drawn in the reconstructed phase difference map, judging by eye the limits of the noisy regions that separate the coherence regions. The left and right limits of each coherence region,  $X_L$  and  $X_R$  are listed in Table 1. The width of the noisy regions is obtained to be 50–60 pixels, and the width of the measurement area is calculated as

**Table 1** Parameters of the temporal coherence areas for Fig. 7 experiments

	$X_L$ (pix)	$x_c$ (pix)	$X_R$ (pix)	$\ell_m$ (mm)
R1	1830	1875	1935	6.9
R2	1640	1710	1780	9.3
R3	1470	1520	1580	7.3
R4	1300	1370	1420	7.9

**Table 2** Nominal and measured  $OPD_{ij}$  for Fig. 7 experiments

	OPD (mm)	Nominal OPD (mm)
R2-R1	10.9	7.7
R4-R3	9.9	7.7
R3-R1	23.5	20.6
R4-R2	22.5	20.6

$X_R - X_L$ . We could expect the four regions to have the same width, as it should be roughly the temporal coherence length, but they are also affected by the intensities of the four reconstructed regions. Thus, a maximum measurement area width of 140 pixels is obtained for  $R_2$ , which corresponds to a maximum measurement length in air  $\ell_m = 9.3$  mm.

For more quantitative information, some phase and intensity profiles have been plotted (Fig. 7c). The phase profile corresponds to the central line ( $Y = 40$  mm) after unwrapping the 2D phase map of Fig. 7b. The intensity profile shows the averaged intensity along most of the fluid height ( $Y = 40 \pm 35$  mm). The intensity averaging has been done taking into account the curvature of the coherence regions. Some rectangles have been drawn in order to show the four different measurement areas, using the  $X_L$  and  $X_R$  values listed in Table 1. Outside these rectangles, the phase is noisy and the intensity is very low. A visual extrapolation of the phase plots for two consecutive areas ( $R_i$  and  $R_{i+1}$ ) to the noisy region between them, shows the phase jumps. The phase jump between the  $R_1$  and  $R_2$  regions is very clear, with the phase being bigger on the left area ( $R_2$ ) than on the right one ( $R_1$ ). The same thing occurs for the other two phase jumps, although it is not so evident.

Once we know the measurement area length and how to control and measure the  $OPD_{ij}$  between the different reference beams, we can maximize the total measurement region. Ideally, we would like to organize the four reference beams ( $R_1 - R_4$ ) such that the four coherence areas (i.e., four stripes) slightly overlap with each other. However, this is not convenient now as we are going to show in the following.

Figure 8a, b shows the intensity and the phase difference maps obtained when increasing the optical path length for  $R_2$  while keeping  $R_1$  unchanged. For an  $OPD_{1,2}$  of 2.0 mm (case 1), we can see a continuous phase map whose total width has increased a little. For cases 2 and 3 (with an  $OPD_{1,2}$  of 5.6 mm and 7.6 mm, respectively), the total measurement area length increases more significantly but a phase jump appears in the middle. The phase profiles (Fig. 8c) show that the phase corresponding to  $R_2$  (left side of the plot) is bigger than the phase corresponding to  $R_1$ , being the position and value of the phase jump dependent on the  $OPD_{1,2}$  value. For case 4 ( $OPD_{1,2} = 10.6$  mm) the two coherent areas are separated. Now, the phase jump can be appreciated in the phase map although it is not so apparent in the central line profile (Fig. 8c).

These phase jumps are due to a very small difference,  $\Delta\lambda$ , in the wavelengths of lasers  $A$  and  $B$  ( $\lambda_A, \lambda_B$ ). We did not observe this problem before (Palero et al. 2010), so we believe it could have been produced when the lasers were sent to be repaired. The true phase difference value occurs in the null OPD lines (curved central line of each coherence area). As we move along the  $X$ -axis there is an extra

phase contribution (phase shift) due to the wavelength difference  $\Delta\lambda$ , which can be calculated as

$$\Delta\phi_\lambda = \frac{2\pi}{\Lambda_{\text{ef}}} n \Delta x_i, \text{ with } \Lambda_{\text{ef}} = \frac{\lambda_A \lambda_B}{\Delta\lambda} \quad (6)$$

where  $\Lambda_{\text{ef}}$  is known as the effective wavelength in air, and  $\Delta x_i = x - x_{c,i}$  is the distance to the null OPD line. As a result, the phase jumps depend on the OPD between both references such that

$$\phi_{ij} = \frac{2\pi}{\Lambda_{\text{ef}}} OPD_{ij} \quad (7)$$

These phase jumps are consistent with a wavelength difference of  $1.5 \cdot 10^{-2}$  nm. However, we have found that the  $\Delta\lambda$  changes significantly with the working energy of both laser cavities, and therefore for each experimental configuration.

The wavelength difference  $\Lambda_{\text{ef}}$  determines the maximum  $OPD_{ij}$  that produces a negligible phase jump as in case 1. The number of holograms needed to cover our large field with an  $OPD_{ij} = 2$  mm configuration is very high. Thus, another approach has been taken to remove the phase jumps and to compensate the phase shift due to the  $\Delta\lambda$ .

First, let us note there are three beams that add up coherently ( $R_1$ ,  $R_2$  and the object beam) in the overlapped areas. In that case, and due to  $\Lambda_{\text{ef}}$ , the phase difference will depend not only on the object phase difference but also on the three beams relative phase and intensity. There is no such problem if the same region is recorded in two separated holograms: one with  $R_1$  and one with  $R_2$ . In addition, we also have a phase shift between the true and the measured phase differences, whose magnitude is slowly increasing with  $\Delta x_i$  (Eq. 6), i.e., as the reconstructed intensity decreases. Thus, we assume the amplitude is a good estimator of the phase map validity. We propose to use the same strategy as in Eq. (5), and add the complex amplitudes obtained from different holograms in order to obtain a more faithful phase difference map.

For all these reasons, we have discarded the idea of having a continuous measurement region. In order to have an optimum configuration for  $R_1 - R_4$  reference beams, we maximize the measurement area with the four reference beams as in case 4. Then, we record a second separated hologram of the same region, but with a shift of the OPD's so the measurement areas fill the gaps of case 4. The averaged complex amplitude obtained from both recordings provides a continuous phase map without the phase jumps associated to the wavelength difference. The full procedure is detailed in the following section.



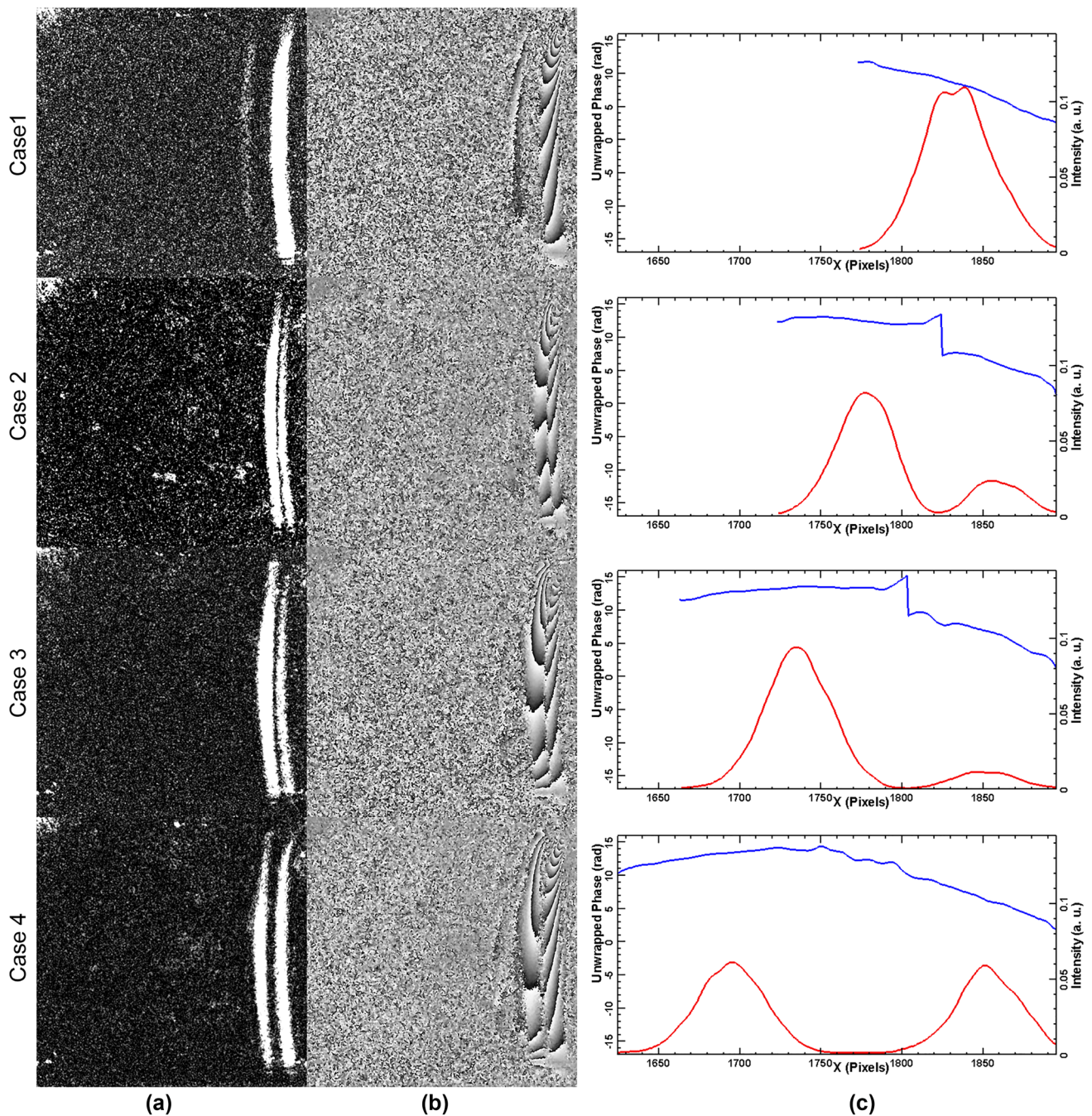


**Fig. 8** Results from four holograms recorded with  $R1$  and  $R2$  for increasingly optical path length differences between them ( $OPD_{1,2}$ ): **a** intensity map **b** filtered phase difference map, **c** averaged line profile

of filtered intensity (red line) and central line profile of filtered phase difference (blue line)

### 3.4 Large field DIPH measurement procedure

Let us now explain the procedure we have developed for measuring the whole fluid plane. We have chosen to introduce an OPD between each reference bigger than our experimental  $\ell_m$ , which was obtained with  $w_1 = 15$  mm and  $w_2 = 40$  mm. As it can be seen in Fig. 7, the total

measurement length in the fluid is close to 30 mm. As the X-length of the fluid plane is 80 mm, it is not possible to measure the velocity field in the whole plane at once, which is not a problem, as the flow is stationary. Thus, we need to adjust the RS global optical path so that it will interfere with consecutive zones of the fluid plane. This adjustment is made by displacing the reference guiding arm output. Only



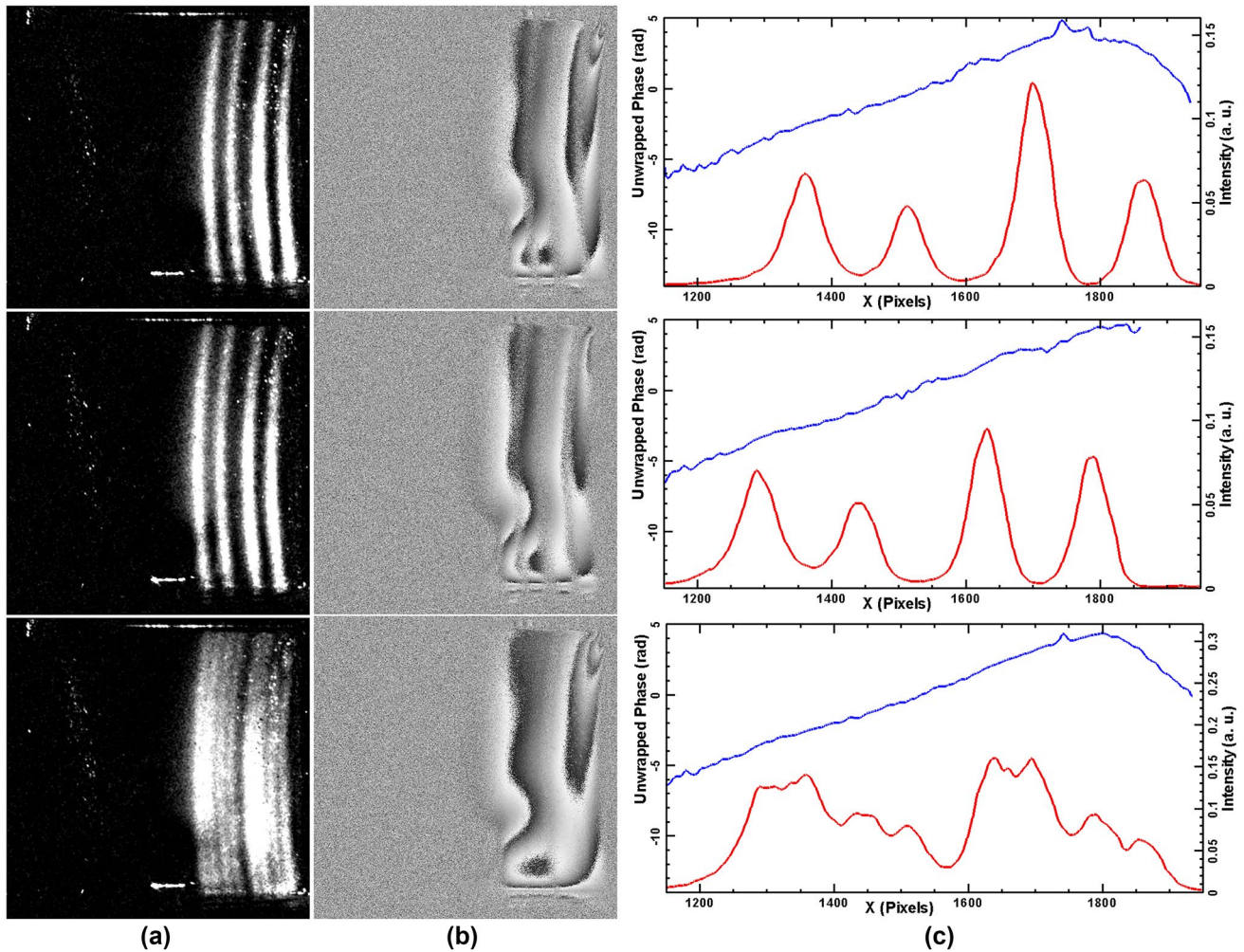


**Fig. 9** Progressive hologram recording and reconstruction for one zone of the fluid plane. Results from two series of holograms (top and middle row) and final results for the zone (bottom row). **a** Intensity

map, **b** phase difference map, **c** averaged line profile of filtered intensity (red line) and central line profile of filtered phase difference (blue line)

three zones are needed to cover the whole plane. For each zone, as explained in the previous section, two hologram sets with small changes in the RS position are recorded.

Results for the first 3 cm region are shown in Fig. 9. In this case, the RS optical path length is adjusted so that it will interfere with the region of the fluid plane nearer to the light entrance. As explained in Sect. 3.2, a series of  $N=20$  hologram pairs (A and B) is recorded and  $\tilde{a}_o(x, y)$  is calculated according to Eq. 5. The second series of holograms have been taken with a 5 mm increase in the RS global optical path. The intensity maps (Fig. 9a, top and middle) and their line profiles (Fig. 9c) show the overlapping of low with high intensity areas from the two series. The phase difference maps (Fig. 9b) show the four regions of coherence, separated by small noisy (no coherence) areas. The central lines profiles for the filtered phase differences (Fig. 9c, top and middle) show these noisy areas as a wavy line (as in Fig. 7c).

The final complex amplitude,  $\tilde{a}_F$ , for the region is calculated from the two  $\tilde{a}_{oi}(x, y)$  as

$$\tilde{a}_F(x, y) = \sum_{i=1}^2 \tilde{a}_{oi}(x, y) \tag{8}$$

As expected, the corresponding phase difference map (Fig. 9b, bottom) and its corresponding filtered phase difference map (Fig. 10c) are continuous and free of noisy region maps. The central line profile for this magnitude (Fig. 9c, bottom) is very smooth, without apparent phase jumps or noisy areas. The resultant intensity is high in the whole region (Fig. 9a, c bottom).

For reconstructing the whole plane, the RS global optical path is adjusted in such a way that it will interfere with the next fluid region, in this case, the center of the flow cavity.

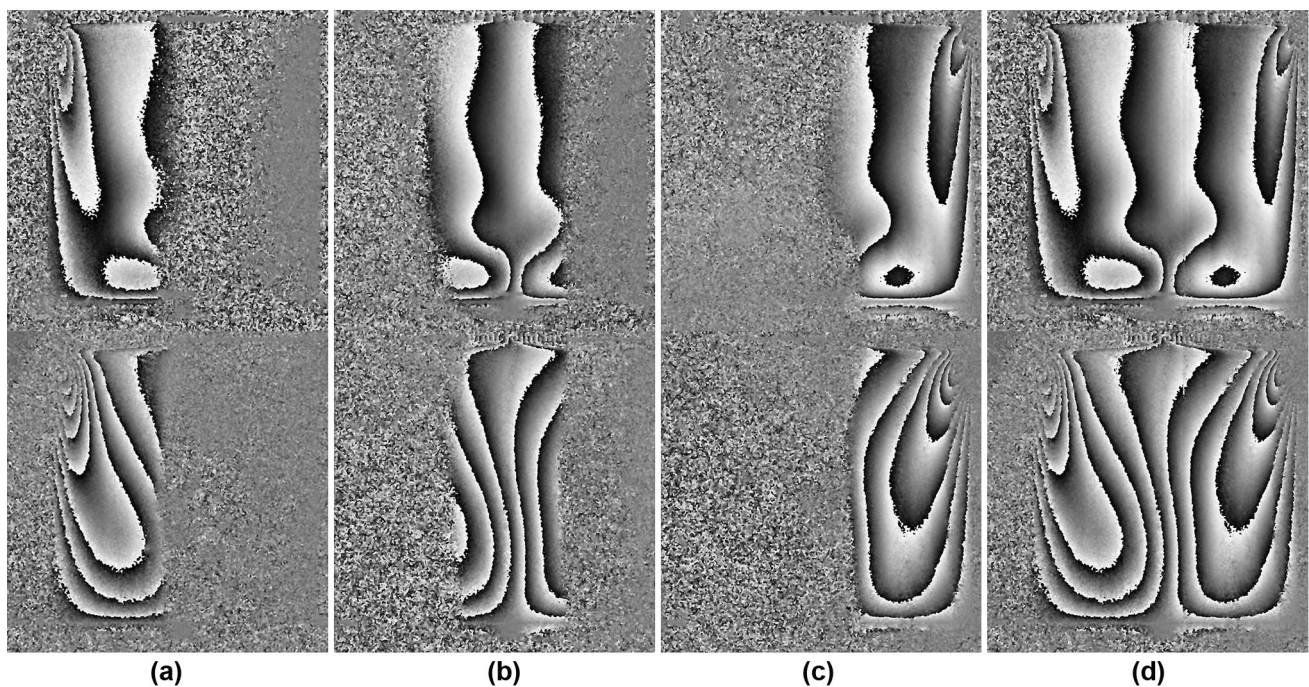


**Fig. 10** Final phase difference maps for (a, b, c) three regions across the fluid plane and (d) the whole fluid plane for  $Re=2000$  (top row) and for  $Re=800$  (bottom row)

Then, the whole procedure described above is repeated for reconstructing this region, obtaining the phase difference maps shown in Fig. 10b. And again the same procedure is repeated to obtain Fig. 10a. As a last step, the  $\tilde{a}_F$  for the three regions are added as in Eq. (8), after zeroing the amplitude in the no coherent (noisy phase) areas, providing the phase difference map for the whole fluid plane (Fig. 10d), where no phase jumps are observed. It is important to remark that good results are obtained even in the area closer to the light output (left side of the images). There, the illumination plane is wider and has lost intensity across the plane due to the particle scattering.

Let us note that the results shown in Fig. 10a–d correspond to  $Re=2000$  (top row), where the hologram pairs were taken with  $\Delta T=5\ \mu\text{s}$ , and to  $Re=800$  (bottom row,  $\Delta T=30\ \mu\text{s}$ ), demonstrating the good performance of the proposed large field DIPH method.

## 4 Results and discussion

Although DIPH holography allows the measurement of the three velocity components, only the out-of-plane component has been obtained from the phase difference values using such a technique. The in-plane components have been measured with PIV, as the holographic reconstructions are noisier than PIV images (Palero et al. (2010)). The reason is that DIPH requires smaller recording lens aperture, which

further reduces the recorded object intensity as compared with a normal PIV image.

Series of PIV images and DIPH holograms were recorded sequentially in experiments with  $Re=2000$  and  $Re=800$ . The in-plane velocity components ( $V_x$  and  $V_y$ ) were measured by correlating pairs of PIV images separated a time interval  $\Delta T_{PIV}$ . The out of plane component was obtained from the phase difference between holograms recorded with a suitable time interval  $\Delta T$ , using an interferometric analysis. In our case,  $\Delta T_{PIV}=2\ \text{ms}$ , while holograms were recorded with  $\Delta T=5\ \mu\text{s}$  for  $Re=2000$  and  $\Delta T=30\ \mu\text{s}$  for  $Re=800$ .

The PIV images were analyzed using DaVis 7.2 (LaVision) software using a multi-pass processing. In the first step the images were analyzed with a window size of  $64\times 64$  pixels and an overlapping of 50%. In the second step the window size was chosen to be  $32\times 32$  pixels also with a 50% of overlapping. The spurious vectors were removed by using a median filter and replaced using a linear interpolation process.

The phase difference maps (Fig. 10d) contain information about the out-of-plane displacement ( $V_z$ ). These are wrapped maps: each fringe represents a  $2\pi$  phase change, but they do not provide any information about the fringe order. Thus, we need to unwrap the phase difference maps (i.e., to assign the correct order to each fringe) so that the absolute phase



**Fig. 11** Normalized iso  $V_z^*$  maps **a** experimental data, **b** numerical simulation data for  $Re = 2000$  (top row) and  $Re = 800$  (bottom row)

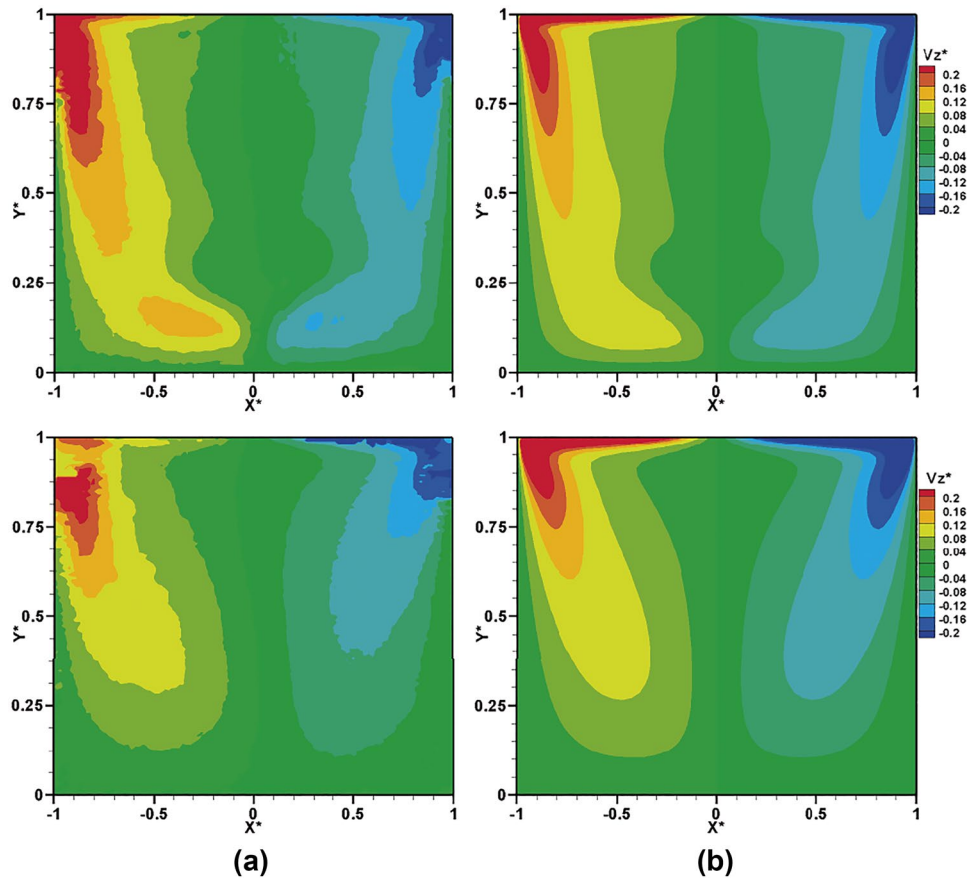


**Fig. 12** Normalized Iso  $V_x^*$  maps **a** experimental data, **b** numerical simulation data for  $Re = 2000$  (top row) and  $Re = 800$  (bottom row)

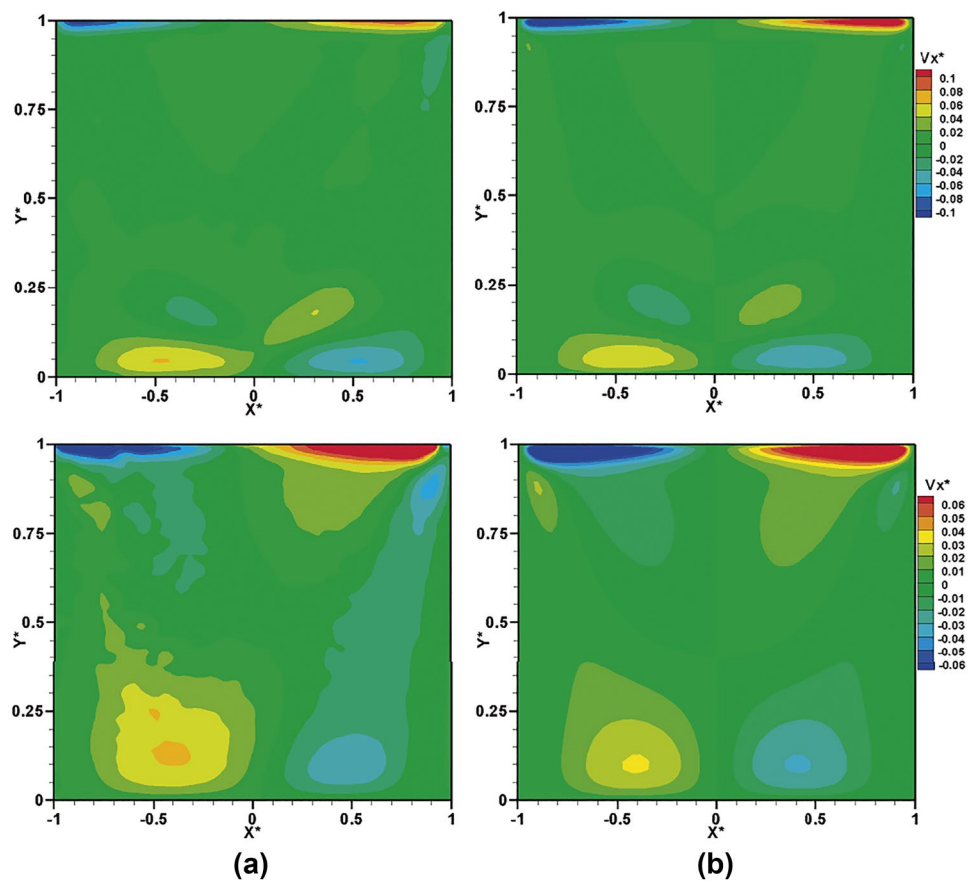
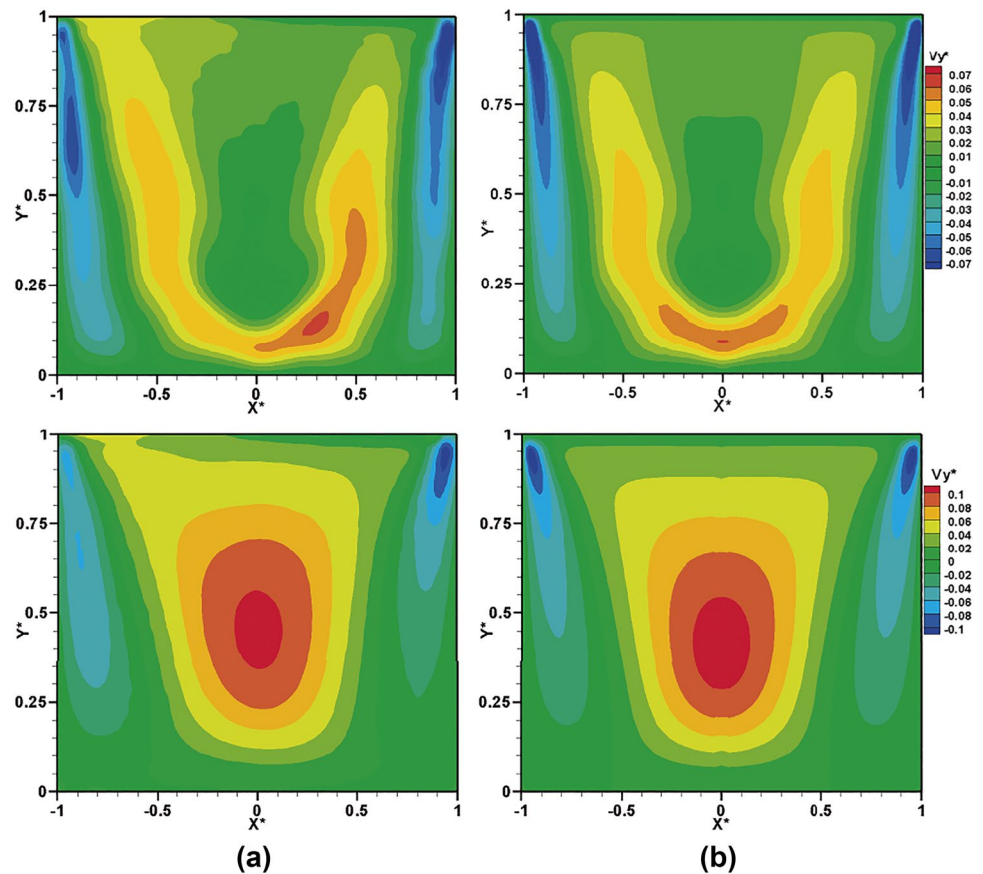




**Fig. 13** Normalized Iso  $V_y^*$  maps **a** experimental data, **b** numerical simulation data for  $Re=2000$  (top row) and  $Re=800$  (bottom row)



difference is known (Palero et al. (2010)). Since the velocities in the flow central axis are zero, we have assigned the zero order to the central fringe in the wrapped maps. From the unwrapped map it is possible to obtain the out-of-plane displacement by using Eq. (4).

The velocity field simulations have been performed with the finite volume commercial code Ansys Fluent v14.0. The SIMPLEC scheme is chosen for the Pressure–Velocity coupling. The spatial discretization for gradient is least squares cell based and for pressure and momentum is second order. The critical Reynolds number for the boundary layer over a rotating disk is about  $Re=3 \cdot 10^5$  (Schlichting and Gersten 2000). In the experiments, the Reynolds number based on the rotation rate and the radius of the disk is relatively low ( $Re=800$  and  $Re=2000$ ), so a laminar stationary solution has been computed. A mesh independence test with three different meshes has been carried out. The meshes are formed by hexahedrons and have boundary layers attached to the walls. A mesh with 0.68 Mnodes has been used for the simulations.

The normalized experimental velocities ( $V_x^*$ ,  $V_y^*$  and  $V_z^*$ ) are compared with the corresponding numerical

simulations (Figs. 11, 12 and 13). The velocity was normalized by a factor of  $\omega R$  ( $Re=2000$ ,  $\omega R=0.93$ ;  $Re=800$ ,  $\omega R=0.35$ ), while the coordinates  $X^*$  and  $Y^*$  were divided by  $R$  (0.04 m) and  $H$  (0.08 m), respectively. Figure 11 shows the  $V_z^*$  obtained experimentally (Fig. 11a) and numerically (Fig. 11b) for  $Re=2000$  (top row) and for  $Re=800$  (bottom row). This velocity component agrees well in both cases, although some asymmetry can be observed, as a higher velocity is obtained in the fluid left side. This asymmetry could be due to a slight misalignment of the rotating cavity lid. For  $Re=800$ , it can be noticed some wrong data in the upper part. These are a consequence of the high velocity gradient occurring in that part of the flow, which leads to the appearance of a large number of interference fringes in the phase difference maps that cannot be solved. Figs. 12 and 13 show the comparison between  $V_x^*$  and  $V_y^*$  obtained from the PIV analysis with the numerical simulation for both Reynolds numbers. Both components agree well.

## 5 Conclusions

A complete procedure for measuring the velocity in a large field of a stationary flow with a laser with short coherence length ( $\ell_c$ ) has been presented. This procedure includes an improved Optical Path Length Enlargement Device (OPLD), that allows the measurement of the out-of-plane velocity component in a fluid plane four times  $\ell_c$ . This improved design allows for an easier and better alignment of the OPLD. In a large field the illumination beam is so much expanded that the laser spatial coherence plays an important role. A more careful adjustment is required and we have proposed a configuration (inverted reference beam), which makes easier and faster the adjustment of the system optical path lengths and improves the final vertical alignment of the four reference beams.

In addition, it has been found that when using a double cavity laser, any wavelength difference between both laser beams will introduce a phase shift in the phase difference map. This drawback has been solved with a new procedure for setting the reference beams and for recording and processing the holograms.

This procedure has been tested in a laminar, confined flow in a cylindrical lid-driven cavity with a rotating end-wall, for two different Reynolds numbers. The comparison of the measured velocity with the numerical simulated data shows a very good agreement for the three velocity components. In conclusion, DIPH together with the OPLD has shown its ability to measure the out-of-plane component in a large area using a laser with a short coherence length.

**Acknowledgements** Spanish Ministerio de Economía y Competitividad (MINECO) and European Commission FEDER program (projects CTQ2013-46799-C2-2-P/1-P and DPI2016-75791-C2-2-P/1-P); Spanish Ministerio de Ciencia e Innovación PID2020-113303GB-C22; Gobierno de Aragón (Laser Optical Technology E44\_17R research group); Universidad de Zaragoza UZ2020-CIE-04

**Author contribution** VP, MPA and JP initiated and supervised the work. AV, JP and IS designed and built the fluid model and performed the CFD calculations. EMR, JL and NA performed the DIPH and PIV measurements. MPA, JL and VP performed the data analysis. The first draft of the manuscript was written by VP. The final version was written by MPA and JL and was read and approved by all the authors.

**Funding** Open Access funding provided thanks to the CRUE-CSIC agreement with Springer Nature.

## Declarations

**Conflict of interest** The authors have no competing interests to declare that are relevant to the content of this article.

**Open Access** This article is licensed under a Creative Commons Attribution 4.0 International License, which permits use, sharing, adaptation, distribution and reproduction in any medium or format, as long as you give appropriate credit to the original author(s) and the source,

provide a link to the Creative Commons licence, and indicate if changes were made. The images or other third party material in this article are included in the article's Creative Commons licence, unless indicated otherwise in a credit line to the material. If material is not included in the article's Creative Commons licence and your intended use is not permitted by statutory regulation or exceeds the permitted use, you will need to obtain permission directly from the copyright holder. To view a copy of this licence, visit <http://creativecommons.org/licenses/by/4.0/>.

## References

- Andrés N, Arroyo MP, Hinrichs H, Quintanilla M (1999) Digital speckle-pattern interferometry as a full-field fluid-velocimetry technique. *Opt Lett* 24:575–577
- Arroyo MP, Greated CA (1991) Stereoscopic particle image velocimetry. *Meas Sci Technol* 2:1181–1186
- Arroyo MP, Hinsch KD (2008) Recent developments of PIV towards 3D measurements. In: Schroder A, Willert CE (eds) *Particle image velocimetry: new developments and recent applications*. Springer, New York, pp 127–154
- Cabeza C, Sarasúa G, Martí AC, Bove I, Varela S, Usera G, Vernet A (2010) Influence of coaxial cylinders on the vortex breakdown in a closed flow. *Eur J Mech B Fluids* 29(3):201–207
- Chen Y, Guildenbecher DR, Hoffmeister KNG, Cooper MA, Stauffacher HL, Oliver MS, Washburn EB (2017) Study of aluminum particle combustion in solid propellant plumes using digital in-line holography and imaging pyrometry. *Combust Flame* 182:225–237
- Denis L, Fournier C, Fournel T, Ducottet C (2008) Numerical suppression of the twin image in in-line holography of a volume of micro-objects. *Meas Sci Technol* 19:074004
- Escudier MP (1984) Observations of the flow produced in a cylindrical container by a rotating endwall. *Exp Fluids* 2:189–196
- Gómez-Climente M, Lobera-Salazar J, Arroyo de Grandes MP, Palero-Díaz V (2022) Three-dimensional particle size and position measurement by linear complex amplitude Wiener filtering. *Opt Express* 30:15008–15023
- Katz J, Sheng J (2010) Applications of holography in fluid mechanics and particle dynamics. *Rev Fluid Mech* 42:531–555
- Kreis T (2005) *Handbook of holographic interferometry: optical and digital methods*. WILEY-VCH Verlag GmbH & Co.KGAA, Weinheim
- Lauterborn W, Kurz K (2003) *Coherent optics: fundamentals and applications*. Springer Science & Business Media
- Lebon B, Perret G, Coëtmelec S, Godard G, Gréhan G, Lebrun D, Brossard J (2016) A digital holography set-up for 3D vortex flow dynamics. *Exp Fluids* 57:103. <https://doi.org/10.1007/s00348-016-2187-8>
- Lobera J, Andrés N, Arroyo MP (2003) Digital image plane holography as a three-dimensional flow velocimetry technique. *Proc. SPIE* 4933:279–284
- Lobera J, Andrés N, Arroyo MP (2004a) Digital speckle pattern interferometry as a holographic velocimetry technique. *Meas Sci Technol* 15:718–724
- Lobera J, Arroyo MP, Perenne N, Stanislas M (2004b) Comparison between PIV & ESPI and stereo PIV on the measurement of 3-C velocity fields; particle image velocimetry: recent improvements. Springer-Verlag, Berlin
- López AM, Lobera J, Andrés N, Arroyo MP, Palero V, Sancho I, Vernet A, Pallarés J (2020) Advances in interferometric techniques for the analysis of the three-dimensional flow in a lid-driven cylindrical cavity. *Exp Fluids* 61:10. <https://doi.org/10.1007/s00348-019-2841-z>
- Ooms T, Koek W, Westerweel J (2008) Digital holographic particle image velocimetry: eliminating a sign-ambiguity error and a bias

- error from the measured particle field displacement. *Meas Sci Technol* 19:074003
- Palero V, Andrés N, Arroyo MP, Quintanilla M (2000) Holographic interferometry vs stereoscopic PIV for measuring out-of-plane velocity fields in confined flows. *Meas Sci Technol* 11:655–666
- Palero V, Lobera J, Arroyo MP (2005) Digital image plane holography (DIPH) for two-phase flow diagnostics in multiple planes. *Exp Fluids* 39:397–406
- Palero V, Arroyo MP, Soria J (2007) Digital holography for micro-droplet diagnostics. *Exp Fluids* 43:185–195
- Palero V, Lobera J, Arroyo MP (2010) Three-component velocity field measurement in confined liquid flows with high speed digital image plane holography. *Exp Fluids* 49:471–483
- Palero V, Lobera J, Andrés N, Arroyo MP (2014) Shifted knife-edge aperture digital in-line holography for fluid velocimetry. *Opt Lett* 39:3356–3359
- Prasad AK, Adrian RJ (1993) Stereoscopic particle image velocimetry applied to liquid flows. *Exp. Fluids* 15:49–60
- Prasad AK, Jensen K (1995) Scheimpflug stereocamera for particle image velocimetry in liquid flows. *Appl. Opt* 34:7092–7099
- Raffel M, Willert C, Kompenhans J (1998) Particle image velocimetry, a practical guide. Springer Verlag
- Rastogi PK (1994) Holographic interferometry: principles and methods. Springer-Verlag, Berlin
- Sancho I, Varela S, Vernet A, Pallarés J (2016) Characterization of the reacting laminar flow in a cylindrical cavity with a rotating endwall using numerical simulations and a combined PIV/PLIF technique. *Int J Heat Mass Transf* 93:155–166
- Schlichting H, Gersten K (2000) *Boundary-Layer Theory*. Springer Science & Business Media
- Schnars U, Jüptner W (2005) *Digital holography*. Springer
- Shankar PN, Deshpande MD (2000) Fluid mechanics in the driven cavity. *Annu Rev Fluid Mech* 32:93–136
- Sheng J, Malkiel E, Katz J (2003) Single beam two-views holographic particle image velocimetry. *Appl Opt* 42:235–250
- Sørensen JN, Naumov I, Mikkelsen R (2006) Experimental investigation of three-dimensional flow instabilities in a rotating lid-driven cavity. *Exp Fluids* 41:425–440
- Spohn A, Mory M, Hopfinger EJ (1998) Experiments on vortex breakdown in a confined flow generated by a rotating disc. *J Fluid Mech* 370:73–99
- Toloui M, Mallery K, Hong J (2017) Improvements on digital inline holographic PTV for 3D wall-bounded turbulent flow measurements. *Measure Sci Technol*. <https://doi.org/10.1088/1361-6501/aa5c4d>
- Verrier N, Atlan M (2011) Off-axis digital hologram reconstruction: some practical considerations. *Appl. Opt* 50:H136–H146

## Authors and Affiliations

Julia Lobera<sup>1</sup> · M<sup>a</sup> Pilar Arroyo<sup>1</sup> · Eva M<sup>a</sup> Roche<sup>1</sup> · Nieves Andrés<sup>1</sup> · Irene Sancho<sup>2</sup> · Antón Vernet<sup>2</sup> · Jordi Pallarés<sup>2</sup> · Virginia Palero<sup>1</sup> 

<sup>1</sup> Instituto de Investigación en Ingeniería de Aragón (I3A), Universidad de Zaragoza, 50009 Zaragoza, Spain

<sup>2</sup> Departamento de Ingeniería Mecánica, Universitat Rovira I Virgili, Campus Sescelades, 43007 Tarragona, Spain